ЖЭТФ, 2025, том 168, вып. 2 (8), стр. 208–214

DETECTION OF TERAHERTZ RADIATION WITH THE p-n GRAPHENE GRID

S. R. Yegiyan [a], ***O. A. Klimenko*** [a,b], ***V. N. Antonov*** [a]

[a] *Skolkovo Institute of Science and Technology*
121205, Moscow, Russia

[b] *Lebedev Physical Institute of Russian Academy of Sciences*
119991, Moscow, Russia

Received January 27, 2025
revised version May 26, 2025
Accepted for publication June 16, 2025

We developed a cryogenic graphene detector for the sub-THz range. Two types of detection operation are envisaged: the bolometeric and the photovoltaic. We find that the leading mode of operation is bolometric. The epitaxial graphene on SiC used in the detector has a strong temperature-dependent weak localization correction to the conductance below 25 K. The sub-THz radiation elevates the temperature of the electron system in the graphene, and thus suppresses the weak localization. No photovoltaic effect is detected. The responsivity of the detector reaches $R \sim 1{\cdot}10^{-3}$ A/W below 1 K.

DOI: 10.31857/S0044451025080097

1. INTRODUCTION

Graphene has flat absorption of electromagnetic radiation across a wide spectral range from the far-infrared (FIR) to visual light. There are two main absorption mechanisms, direct Drude absorption by electrons and excitation of plasma waves in two-dimensional electron gas (2DEG) [1–3]. These excitations can stay in the electron system for a long time and propagate to a large distance because of the weak coupling to the phonon bath [4]. Drude absorption heats the 2DEG so that the operation of the detector would be bolometric type [5,6]. Epitaxial graphene at cryogenic temperatures has a strong temperature-dependent weak localization (WL) correction to the conductance: it decreases by more than 20 % from 25 K to 0.5 K [7–11]. Once the 2DEG is heated by the absorbed radiation, the WL correction is suppressed, resulting in photocurrent when the constant bias voltage is applied. The bolometer does not have any spectral sensitivity, unless the coupling antenna is designed for a particular wavelength. The bolometric effect can be strongly enhanced by patterning the graphene layer. The formation of quantum dots provides an effective way to enhance the dependence of the electrical resistance on the electron temperature due to the quantum confinement gap formation [12–14]. The detector exploiting the second mechanism, the excitation of the plasma waves, requires a nonuniform potential landscape for operation [15]. The excited plasma waves are rectified at this non-uniform potential to produce the photovoltage. The plasmonic detector may have spectral sensitivity when the non-uniform potential is periodic. For example, one can design a detector with a periodic grid of $p-n$ junctions. No bias voltage is required for the operation of the plasmonic detector. This mechanism of photo-response is used in a number of detectors [16–18]. The $p-n$ junctions in graphene can be formed by electrostatic gating or a combination of p- and n-doping metals on the top of the graphene. For example, Ti/Au is known for p-doping of epitaxial graphene graphene, while Pd does the n-doping [19]. The $p-n$ junctions are formed next to metallization. There are also detectors where there is a synergy of two mechanisms, so called a photothermoelectric effect (PTE) [20–24].

Despite the fact that the graphene detectors reported so far concede to the semiconductor ones in sensitivity, they have a higher operation speed. The latter may be the key advantage in some applications, such as integrated photonics. In this work, we study the sub-THz photosensitive operation of the graphene

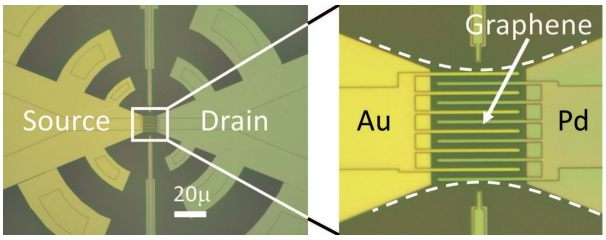

Fig. 1. EpiG photodetector. Graphene stripe of 10 μm wide and 10 μm long is in the focal point of wide band log-periodic antenna, which spans to 2 mm. Graphene elsewhere is etched away. Left and right lobes of the antenna are made of Ti/Au and Pd. There are 0.2 μm wide inter-digitated electrodes of Ti/Au and Pd over the graphene stripe. The antenna lobs serve also as source and drain contacts

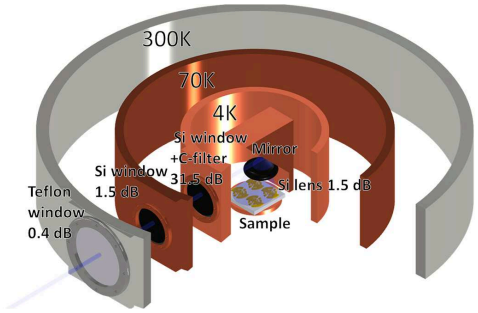

Fig. 2. The optical scheme of the experiment. Teflon and two Si windows at different stages of the refrigerator filters IR radiation incident at the detectors from the room temperature. Finally Si lens focuses THz signal to the detector. Attenuation of the THz radiation by the optical setup is -36 dB

detector at cryogenic temperatures, below 4 K. The detector is designed as a plasmonic type, with a periodic grid of $p-n$ junctions in epitaxial graphene. We expected excitation of the plasma waves and the photovoltaic response with spectral sensitivity. However, in the experiment, we predominantly observe the bolometric effect. The responsivity of the detector is rather low $R \sim 1{\cdot}10^{-3}$ A/W.

2. EXPERIMENTAL RESULTS

2.1. Design of photodetector

The detector is made of epitaxial graphene synthesized on the Si-terminated face of the SiC (SiC/G). There are two layers of graphene on SiC surface: the bottom one is strongly coupled to the Si-terminated face of SiC (non-conductive), and the top one is weakly coupled to SiC (conductive, n-doped) [25]. The carrier concentration and mobility of SiC/G are $n_{\mathrm{SiC/G}} = 5 \cdot 10^{11}$ cm^{-2} and $\mu_{\mathrm{SiC/G}} = 7500$ cm^2/Vs respectively. Two materials, Ti/Au and Pd, form p- and n-doping in graphene. The work functions of Au and Pd are close to each other, 4.13 eV and 5.12 eV, respectively. However, their interaction with SiC/G is quite different. It is well known that the intercalation of Au between the two graphene layers grown on SiC makes it possible to achieve a p-doped graphene state [19]. It is the result of the diffusion of Au to SiC/G. The Pd does not diffuse to SiC/G and works as a usual metallic n-dopant. There is also thin Ti (the work function $3.9-4.3$ eV depending on the quality) film, which is used for better adhesion of Au. Such a thin Ti film allows gold to diffuse to the SiC/G.

There are a number of steps needed to fabricate samples. The Ti(5 nm)/Au(50 nm) and Pd(50 nm) fine patterns of the inter-digitated electrodes are consecutively exposed with the Electron Beam Lithography system and deposited using the thermal e-gun evaporator, see the right panel of Fig. 1. Then the Ti(5 nm)/Au(100 nm) and Pd(100 nm) lobs of the log-periodic antenna are fabricated using the same technology, the left panel of Fig. 1. Finally, the graphene film outside the 10 μm wide stripe between the antenna lobs is etched away in the oxygen plasma. The PMMA resist mask is used to protect the graphene pattern during the last step. The resist mask is dissolved in acetone after the etching. SiC/G continues under the metal, so we expect p- and n-doping of the graphene in the vicinity of the inter-digitated electrodes. In such a design, we expect p-doping under the Ti/Au electrodes, n-doping under the Pd electrodes. In between the electrodes, SiC/G remains n-doped.

When designing the detector we plan to resonantly excite the plasma waves in the graphene with the wave vector q:

$$q = \frac{1}{L\sqrt{\varepsilon_{eff}}}, \tag{1}$$

where L is the period of inter-digitated electrodes and $\varepsilon_{eff} = (\varepsilon_{\mathrm{SiC}} + 1)/2$ is an effective dielectric constant of the SiC/G. At the sub-THz frequencies $\varepsilon_{\mathrm{SiC}} \sim 6.5$, and, correspondingly, $\varepsilon_{eff} = 3.76$. The dispersion relation of the plasmons in graphene in the limit of large q is

$$\omega = \frac{1}{\hbar}\sqrt{\frac{2\varepsilon_0\varepsilon_{eff}}{e^2 g_s g_v E_F}\,q} \tag{2}$$

with $g_s = 2$ and $g_v = 2$ to be spin and valley degeneracies. For $L = 0.2$ μm in our detector one expects $\sim$0.4 THz. The resonance of the plasma waves in the 1 μm wide graphene stripes with the carrier concentration $1.5{\cdot}10^{13}$ cm^{-2} was demonstrated at ~ 6 GHz [26]. We normalize carrier concentration and stripe width in

our detector to that data in accordance with (2) and get slightly smaller resonance frequency 0.24 THz. The latter is closer to the CW of our THz source.

2.2. Measurement setup

For assessment of the photosensitive operation in the terahertz range, we cool the detector to helium temperature, down to 0.5 K. The detector is enclosed in the metal cooper box attached to the cold head of a dry refrigerator. The radiation from the room temperature environment delivered to the detector is filtered with the teflon lense at 300 K, Si window at 77 K, Si window with neutral carbon filter at 4 K, and the black polyethylene filter and Si lens at the cooper box window, Fig. 2. The black polyethylene filter has weak transparency above few THz. Behind the black polyethylene filter there is a semi-spherical Si lens that focuses radiation to the face of the detector. The 0.177 THz source with δf ∼1 GHz and maximum power of 2 mW is located at room temperature. We estimate the attenuation the optical system ∼35 dB. This includes Teflon window (0.4 dB), two Si windows (1.5 dB each), neutral carbon filter (30 dB) and Si lens (1.5 dB). The maximum incident on the area of the log-periodic antenna of the detector is 600 nW. The radiation is modulated at room temperature with a chopper of f_{mod} ∼33 Hz. The current of the detector is demodulated at f_{mod} to obtain the photo-response.

2.3. Photo sensitive operation

The temperature dependence of SiC/G resistance is non-monotonous with a steep rise below 20 K, see Fig. 3 *a*. The resistance increases from ∼5.6 kΩ at 20 K to ∼22 kΩ at 0.9 K. The latter is explained by the WL and electron-electron (EE) interaction effect in the Epi graphene below 20 K [7, 11]. The effects are rather strong because of large phase breaking and thermal lengths at low temperatures. The main source of the inelastic scattering of the electron are donors on SiC surface. The $I-V$ curve at 1 K has a slight nonlinearity, see the insert in Fig. 3 *a*.

The photocurrent depends on the bias voltage, V_b. It reaches the minimum close to zero bias, and increases with the V_b, the Fig. 3 *b*. The photocurrent saturates at the bias of V_b ∼1 mV. The maximum of photocurrent linearly increases with the incident power and saturates above 0.5 μW (see Fig. 4 *a*). The responsivity of the detector is R ∼$1{\cdot}10^{-3}$ A/W. In the calculations of R we use the quantum efficiency of 0.01.

The noise-equivalent power (NEP) is estimated from the photocurrent measurements with the radiation source attenuated by −36 dB, so that the photosignal is equal to the noise level. The lock-in time constant is set to 0.5 s (0.5 Hz bandwidth). Thus,

$$NEP \approx 0.6\mu\text{W}/(4000 \cdot \sqrt{0}.5\text{Hz}) \approx$$

$$\approx 2 \cdot 10^{-10}\text{W}/\sqrt{\text{Hz}}.$$

At a high bias voltage, $V_b > 1$ mV, the photocurrent fluctuates by ∼10%. When the temperature increases, the minimum photoresponse stays in the vicinity of V_b= 0 V up to 2.5 K, and then shifts to positive bias (Fig. 5 *b*). The slope of the photoresponse curve becomes less steep, the amplitude decreases, but the saturation bias voltage becomes larger (Fig. 5 *a*). There are fluctuations of the photocurrent at zero bias when the incident THz flux increases (Fig. 4 *b*).

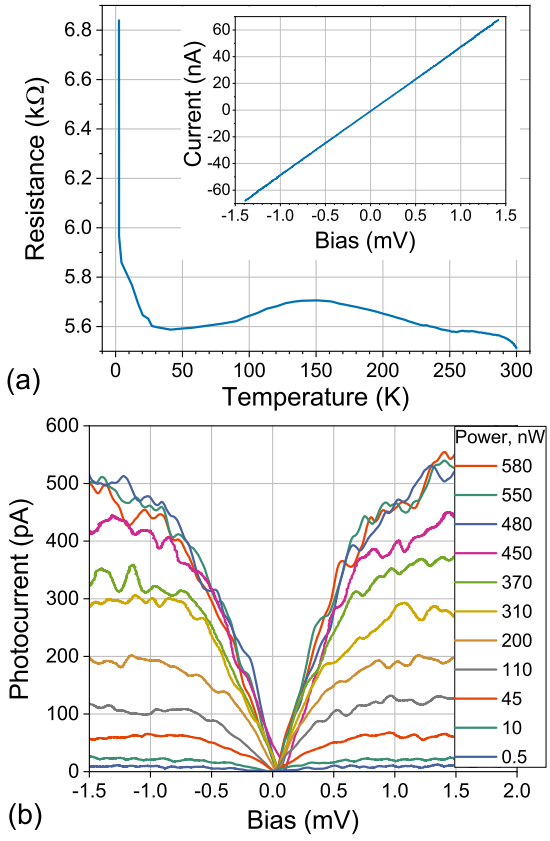

Fig. 3. *a* — Temperature dependence of the SiC/G resistance. The insert: $I-V$ curve at $T = 0.9$ K. There is a slight nonlinearity of the $I-V$ curve due to formation of the $p-n$ junctions. *b* — Absolute value of the photocurrent at different incident power

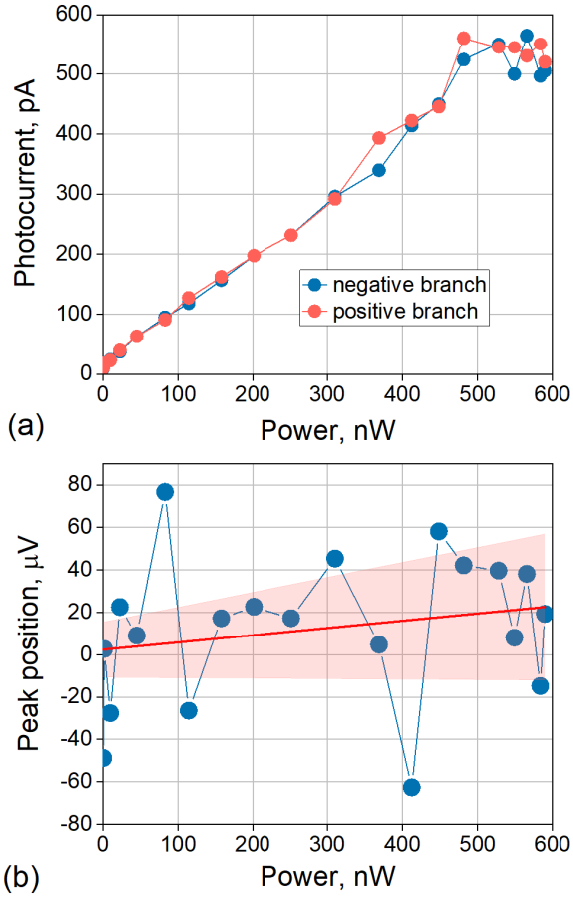

Fig. 4. *a* — The photocurrent taken at 1.5 mV bias voltage. Red and blue dots correspond to the negative and positive voltage bias. *b* — Position of the photocurrent minimum at different power of the incident radiation. The experimental data (blue dots) has the linear fit (red line) with gradient 34 nW/μV (the shadow indicates the fit confidence corridor)

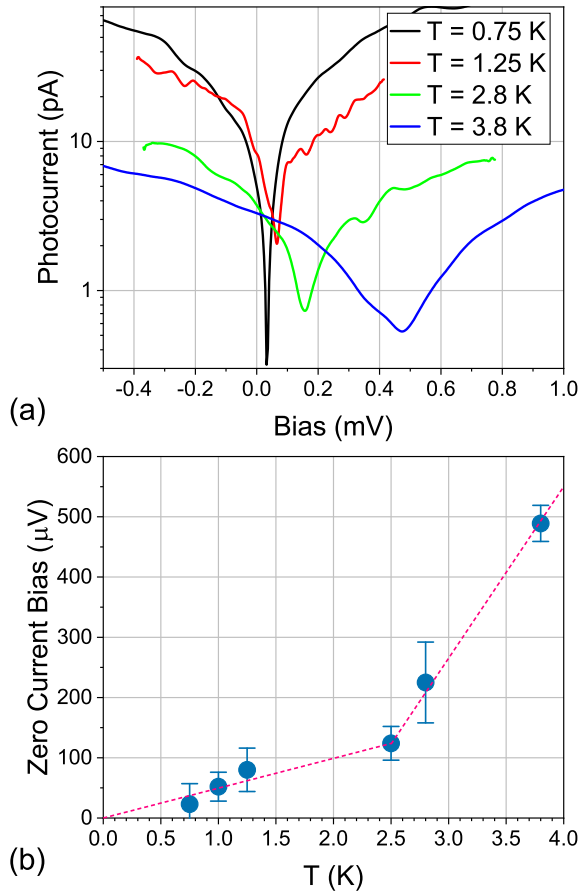

Fig. 5. *a* — Photocurrent at different temperatures. The minimum of the photocurrent shifts with the temperature. *b* — The position of the photocurrent minimum at different temperatures

3. DISCUSSION

The photoresponse of the graphene to the THz radiation has been studied in a number of works. We compare our results with two of them [7, 16]. The design of the THz detectors in both cases is very similar to each other. The difference is in the original material: the SiC/G was used in the first work, and the exfoliated graphene in the second. The bolometric effect is observed in the SiC/G detector, and the excitation and decay of the plasmons in the detector with exfoliated graphene. The difference in effect is highly probable to be the result of a low mobility and low carrier concentration of the SiC/G compared to that of the exfoliated graphene. They were $n_{\mathrm{SiC/G}} = 5 \cdot 10^{11}$ cm^{-2} $\mu_{\mathrm{SiC/G}} = 7500$ cm$^2/Vs$ in SiC/G and $n_G = 10^{12}$ cm^{-2} and $\mu_G = 10^6$ cm$^2/Vs$ in exfoliated graphene at $T \sim 10K$. To excite plasmons one needs high carrier concentration and high mobility. Otherwise, the only photon absorption mechanism is the Drude absorption with heating of the electronic system. The WL and EE corrections to the conductance then decay with the temperature, which is seen as the photoresponse.

It is likely that the Drude absorption is the leading mechanism in the current experiment also. First of all, the responsivity R is relatively low compared to the experiments with plasmon excitation [16]. Also, the photocurrent is bias dependent: it increases from almost zero to the saturation with the bias voltage. The behavior is consistent with the model where the conductance changes due to suppression of the WL and EE under the THz radiation. The maximum amplitude should be then limited by the value of the WL

and EE. Once they are suppressed at high temperatures of the electron system, the photocurrent should saturate.

Alternating graphene doping by Ti/Au and Pd lobs of the log-periodic antenna also leads to inhomogeneous heating of charge carriers required for the PTE effect. The PTE contribution to the photocurrent is given by [23, 27, 28] $j_{PTE} = \sigma S \nabla T_e$, where σ is the graphene conductivity, S is the Seebeck coefficient and T_e is the electron temperature, so the PTE photocurrent does not depend on the bias. Since the photocurrent as a function of bias consists of two plateaus at negative and positive bias and a drop to zero near zero bias (see Fig. 3 *b*.), the PTE effect would manifest as (1) a systematic shift of the photocurrent minimum sidewards accompanied by (2) a counter-directional shift of the plateaus: upwards and downwards. At 0.9 K, there are fluctuations of minimum photocurrent with the incident power, but the confidence corridor of its linear fit covers zero peak position. So that the deviation of the minimum photocurrent from zero is statistically indistinguishable (Fig. 4 *b*). When increasing temperature to 3.8 K, the photocurrent minimum shifts towards the positive bias. However the plateaus descend keeping equal photocurrent level (Fig. 5 *a*). Thus, we may conclude that the PTE effect has no remarkable impact on the photocurrent because of a small Seebeck coefficient, $< 1\ \mu V/K$ at $T < 4\ K$ [28], and weak incident radiation.

The plasmonic contribution to the photocurrent may occur via two mechanisms in our structures. There can be excitation and decay of the plasmons between neighboring Ti/Au and Pd electrodes, which is usually seen as a *dc* voltage induced under THz radiation [16, 29]. The effect should appear as a sideward shift of the photocurrent minimum with the THz intensity. We do not see this in the experiment (Fig. 3 *b*). At a particular bias voltage the periodic inter-digital electrodes can form also a resonant plasmonic nanostructure for the incident radiation [30, 31]. The plasmonic enhancement of the photo-response would appear as resonant peaks at particular bias values, when the plasmon frequency matches the incident radiation's one. However, no such resonances at non-zero bias are registered (Figs. 4 *a*, 5 *a*).

To estimate the bandwidth of the detector we take into account the time constant $\tau = RC$ and time of diffusion electrons/plasmons between the interdigital metal electrodes. The resistance of the graphene stripe, $R \sim 6.8$ kΩ, and capacitance of the log-periodic antennae, $C \sim 1$ pF gives $\tau \sim 6$ nsec, and the corresponding bandwidth is 150 MHz. The bandwidth determined by the time of diffusion of the electrons/plasmons is much higher, > 1 THz (electron velocity in graphene $\sim 10^6$ m/s, travel distance ~ 1 μm). To increase the bandwidth, one has to redesign the detector. In particular, a wide-band log-periodic antenna can be replaced with a resonant dipole antenna, the size of which can be much smaller. It is also possible to reduce R by changing the geometry of the graphene strip.

The temperature evolution of the photoresponse can not be fully explained by the bolometric effect, see (Fig. 5). The photocurrent minima shift to the positive bias voltage, when the temperature is above 2 K. The data are taken at constant 0.6 μW incident THz power. The shift reaches 0.5 mV at 3.7 K, whereas left and right branches of the photocurrent remain symmetric about the minimum. The shift cannot be caused by plasmon-related detection as then there should be a correlated shift of minima up/down by the value of exceeding observed on by two orders of magnitude. A possible explanation of this shift is the thermovoltaic effects in metal-graphene contacts, or current/voltage leads. Thus, the graphene-metal contact resistance increases with temperature below 20K. It is a consequence of the change in the electron transmission from metal to metal-doped graphene. The latter is governed by the ratio of the mean free path in graphene under the metal and the length of the metal–graphene coupling, which are both temperature dependent [32–34].

4. CONCLUSION

In conclusion, we explore the SiC/G-based cryogenic THz detector. The design of the detector intended to utilize plasmon excitation and rectification in SiC/G stripe with inter-digitated thin film fingers of Pd and Ti/Au. Only the bolometric photoresponse is observed. The photoresponse is a suppression of the two quantum corrections to the conductance (WL and EE) when the temperature of the electron system is elevated by the THz absorption. However, the responsivity of this detector is relatively low $R \sim 1 \cdot 10^{-3}$ A/W. We believe that graphene with higher mobility and higher carrier concentration is needed for the operation of the detector in the plasmonic mode.

Acknowledgment. The authors thank Dr. A. V. Bubis for his valuable experimental support and fruitful discussions. S. R. Yegiyan acknowledges support from the Skoltech Next Generation Program grant №1-NGP-1064, and O. A. Klimenko acknowledges support from the RSF grant № 25-29-00544.

REFERENCES

1. T. Low and P. Avouris, *Graphene Plasmonics for Terahertz to Mid-Infrared Applications*, ACS Nano **8**, 1086 (2014).

2. P. Rufangura, T. G. Folland, A. Agrawal et al., *Towards Low- Loss On-Chip Nanophotonics With Coupled Graphene and Silicon Carbide: A Review*, J. Phys.: Materials **3**, 032005 (2020).

3. Q. Guo, C. Li, B. Deng et al., *Infrared Nanophotonics Based on Graphene Plasmonics*, ACS Photonics **4**, 2989 (2017).

4. M. B. Lundeberg, Yu. Gao, A. Woessner et al., *Thermoelectric Detection and Imaging of Propagating Graphene Plasmons*, Nature Materials **16**, 204 (2016).

5. F. Xia, T. Mueller, R. Golizadeh-Mojarad et al., *Photocurrent Imaging and Efficient Photon Detection in a Graphene Transistor*, Nano Lett. **9**, 1039 (2009).

6. T. Mueller, F. Xia and P. Avouris, *Graphene Photodetectors for High-Speed Optical Communications*, Nature Photonics **4**, 297 (2010).

7. V. Eless, T. Yager, S. Spasov et al., *Phase Coherence and Energy Relaxation in Epitaxial Graphene Under Microwave Radiation*, Appl. Phys. Lett. **103**, 093103 (2013).

8. A. Fujimoto, C. J. Perini, D. Terasawa et al., *Disorder and Weak Localization Near Charge Neutral Point in Ti-cleaned Single-Layer Graphene*, Phys. St. Sol. (B) **256**, 1800541 (2019).

9. E. McCann, K. Kechedzhi, V. I. Fal'ko et al., *Weak-Localization Magnetoresistance and Valley Symmetry in Graphene*, Physical Review Letters **97**, 146805 (2006).

10. R. Somphonsane, H. Ramamoorthy, G. He et al., *Universal Scaling of Weak Localization in Graphene Due to Bias-Induced Dispersion Decoherence*, Sci. Rep. **10**, 5611 (2020).

11. S. Lara-Avila, A. Tzalenchuk, S. Kubatkin et al., *Disordered Fermi Liquid in Epitaxial Graphene from Quantum Transport Measurements*, Phys. Rev. Lett. **107**, 166602 (2011).

12. A. El Fatimy, R. Myers-Ward, A. Boyd et al. *Epitaxial Graphene Quantum Dots for High-Performance Terahertz Bolometers*, Nature Nanotech **11**, 335 (2016).

13. A. El Fatimy, P. Han, N. Quirk et al. *Effect of Defect-Induced Cooling on Graphene Hot-Electron Bolometers*, Carbon **154**, 497 (2019).

14. A. El Fatimy, A. Nath, B. D. Kong et al., *Ultra-Broadband Photodetectors Based on Epitaxial Graphene Quantum Dots,* Nanophotonics **7**, 735 (2018).

15. P. Kleinschmidt, S. Giblin, A. Ya. Tzalenchuk at al., *Sensitive Detector for a Passive Terahertz Imager*, J. Appl. Phys. **99**, 114504 (2006).

16. D. Bandurin, D. Svintsov, I. Gayduchenko et al., *Resonant Terahertz Detection Using Graphene Plasmons*, Nature Communications **9**, 5392 (2018).

17. D. Mylnikov and D. Svintsov, *Limiting Capabilities of Two-Dimensional Plasmonics in Electromagnetic Wave Detection*, Phys. Rev. App. **17**, 064055 (2022).

18. P. Ma, Ya. Salamin, B. Baeuerle et al., *Plasmonically Enhanced Graphene Photodetector Featuring 100 Gbit/s Data Reception, High Responsivity, and Compact Size*, ACS Photonics **6**, 154 (2018).

19. Y. C. Cheng and U. Schwingenschlögl, *A Route to Strong -Doping of Epitaxial Graphene on SiC*, Appl. Phys. Lett. **97**, 193304 (2010).

20. F. Ludwig, A. Generalov, J. Holstein et al., *Terahertz Detection with Graphene FETs: Photothermoelectric and Resistive Self-Mixing Contributions to the Detector Response*, ACS Appl. Electron. Mat. **6**, 2197 (2024).

21. X. Cai, A. B. Sushkov, R. J. Suess et al., *Sensitive Room-Temperature Terahertz Detection via the Photothermoelectric Effect in Graphene*, Nature Nanotechnology **9**, 814 (2014).

22. X. Xu, N. M. Gabor, J. S. Alden et al., *Photo-Thermoelectric Effect at a Graphene Interface Junction*, Nano Let. **10**, 562 (2009).

23. S. Castilla, B. Terres, M. Autore et al., *Fast and Sensitive Terahertz Detection Using an Antenna-Integrated Graphene pn Junction*, Nano Lett. **19**, 2765 (2019).

24. N. M. Gabor, J. C. W. Song, Q. Ma et al., *Hot Carrier–Assisted Intrinsic Photoresponse in Graphene*, Science **334**, 648 (2011).

25. J. A. Alexander-Webber, J. Huang, D. K. Maude, at al., *Giant Quantum Hall Plateaus Generated by Charge Transfer in Epitaxial Graphene*, Sci. Rep. **6**, 30296 (2016).

26. Long Ju, B. Geng, J. Horng, C. Girit, M. Martin, Z. Hao, H. A. Bechtel, X. Liang, A. Zettl, Y. R. Shen, F. Wang, *Graphene Plasmonics for Tunable Terahertz Metamaterials*, Nature Nanotechnology **6**, 630 (2011).

27. J. C. W. Song, M. S. Rudner, C. M. Marcus, and L. S. Levitov, *Hot Carrier Transport and Photocurrent Response in Graphene*, Nano Lett. **11**, 4688 (2011).

28. E. H. Hwang, E. Rossi, and S. Das Sarma, *Theory of Thermopower in Two-Dimensional Graphene*, Phys. Rev. B **80**, 235415 (2009).

29. T. A. Elkhatib, V. Yu. Kachorovskii, W. J. Stillman et al., *Enhanced Plasma Wave Detection of Terahertz Radiation Using Multiple High Electron-Mobility Transistors Connected in Series*, IEEE Transactions on Microwave Theory and Techniques **58**, 331 (2010).

30. T. J. Echtermeyer, L. Britnell, P. K. Jasnos et al., *Strong Plasmonic Enhancement of Photovoltage in Graphene*, Nature Communications **2**, 458 (2011).

31. E. G. Mishchenko, A. V. Shytov and P. G. Silvestrov, *Guided Plasmons in Graphene p–n Junctions*, Phys. Rev. Lett. **104**, 156806 (2010).

32. G. Giovannetti, P. A. Khomyakov, G. Brocks et al., *Doping Graphene with Metal Contacts*, Phys. Rev. Lett. **101**, 026803 (2008).

33. F. Xia, V. Perebeinos, Yu. Lin et al., *THe Origins and Limits of Metal–graphene Junction Resistance*, Nature Nanotechnology **6**, 179 (2011).

34. T. Cusati, G. Fiori, A. Gahoi et al., *Electrical Properties of Graphene-Metal Contacts*, Sci. Rep. **7**, 5109 (2017).